Eur. Phys. J. B **4**, 269–277 (1998)

THE EUROPEAN PHYSICAL JOURNAL B

Optical and paramagnetic properties of titanium centres in ZnS

J. Dziesiaty[1], M.U. Lehr[2], P. Peka[2], A. Klimakow[1], S. Müller[1], and H.-J. Schulz[2,a]

[1] Humboldt-Universität zu Berlin, Institut für Physik, Invalidenstrasse 110, 10099 Berlin, Germany
[2] Fritz-Haber-Institut der Max-Planck-Gesellschaft, Faradayweg 4-6, 14195 Berlin, Germany

Received: 3 October 1997 / Revised: 17 December 1998 / Accepted: 18 May 1998

Abstract. ZnS:Ti crystals grown by different methods are investigated at low temperatures (2 K $\leq T \leq$ 80 K) by electron paramagnetic resonance (EPR) and optical spectroscopies, mainly with regard to their photoluminescence properties, including excitation and sensitisation spectra. The more familiar lattice-neutral $Ti^{2+}(d^2)$ ion on a cubic site (AN) presents an isotropic EPR signal with $g = 1.928$ observable up to 80 K. Signals of axial PN and AS sites are detected in the same temperature range. This Ti^{2+} ion exhibits the ${}^3T_2(F) \rightarrow {}^3A_2(F)$ transition in emission, structured by no-phonon lines (NPL) of centres in various environments, with the AN site represented at 3613 cm^{-1}, and the ${}^3T_1(F)$ and ${}^3T_1(P)$ bands in excitation spectra. Substitutional $Ti^{3+}(d^1)$ is identified by an anisotropic EPR spectrum at $T = 3.5$ K, indicating a quasistatic Jahn-Teller effect at the doubly degenerate ${}^2E(D)$ ground state, while in the first excited vibronic state a quasidynamic JT effect in the strain-split vibronic ${}^2E/{}^2A_2$ manifold is found. A new luminescence band centred at 4500 cm^{-1} with NPL structures near 5000 cm^{-1} represents AN, PN and AS sites in the ${}^2T_2(D) \rightarrow {}^2E(D)$ transition. Charge-transfer processes are described in a one-particle model, depicting the Ti^{3+}/Ti^{2+} donor level at 12 900 cm^{-1} below the conduction-band edge.

PACS. 71.70.-d Level splitting and interactions – 76.30.Fc Iron group ($3d$) ions and impurities (Ti-Cu) – 78.55.Et II-VI semiconductors

1 Introduction

While titanium as a dopant in II-VI semiconductors found an early attention regarding its magnetic properties (ZnS: [1]; CdS: [2]; CdTe: [3]), comparatively few papers were published in the meantime, until recently the interest was raised anew by the search for midgap levels, desired in a number of prospective applications. Especially from EPR investigations, titanium was soon known to enter the host lattice substitutionally on a cation site and to assume preferentially the quasi-neutral charge state $Ti^{2+}(d^2)$. Among the earlier optical absorption studies [4,5] were several in which, based on photoconductivity among other facts, the occurrence of excited Ti states degenerate with the conduction band was considered, *e.g.* for CdS [4], ZnSe [6], CdSe [7] and CdTe [8]. With ZnS and ZnSe, an antiresonance of TO(Γ)-coupled states with Jahn-Teller vibrational states was unveiled [9]. In 1994, luminescence of titanium impurites was detected, thus also enabling studies of changes of the Ti charge states. For instance, $Ti^{3+}(d^1)$ was discovered in ZnSe [10], and as well in CdTe and (Cd,Zn)Te ternary compounds [11]. Especially ZnSe:Ti was thoroughly investigated by a combination of EPR and optical methods, including the influence of intriguing Jahn-Teller interactions [12].

It is the aim of the present study to extend the previous results to ZnS, a material which by virtue of its wide band gap is especially apt to open an insight into optically-induced charge-transfer processes. The properties of Ti^{3+} will here turn out as similar to those of ZnSe:Ti, especially with respect to vibrational interactions. On the other hand, the charge-conversion processes reveal some characteristic features by comparison between various II-VI materials.

2 Experimental methods

In an attempt to grow homogeneous ZnS:Ti specimens with different titanium concentrations, two techniques were employed, *viz.* post-growth diffusion annealing of pure crystalline ZnS slices (see a and b below) and *in-situ* doping by co-evaporation of ZnS and TiS_2 from separate sources (group c below):

a) A nearly wholly cubic ZnS crystal (hexagonal part smaller than 2%) of 1 mm thickness was sealed off with a ZnS + TiS_2 mixture in a quartz ampoule under 53 kPa Ar. The TiS_2 concentration in the basic mixture was 1.5 mol%. After seven days annealing at 1400 K, the ampoule was quenched in water.

---

[a] e-mail: `schulz@fhi-berlin.mpg.de`

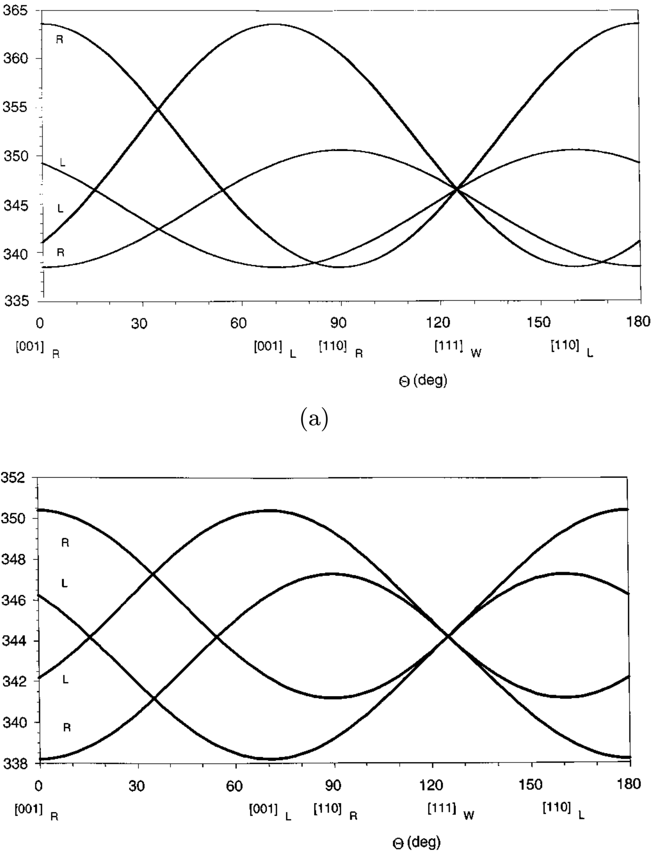

(a)

(b)

Fig. 1. Angular dependence of $Ti^{3+}(d^1)$ EPR signal in the {110} plane, (a) static and (b) dynamic limit, averaged line omitted. R and L label the twin spectra.

b) A corresponding material with a different doping level was aimed at, by starting from a mixture with 0.3 mol% nominal TiS_2 content, this time annealed at 1330 K.

c) In seeded chemical vapour-transport growth in hydrogen (SCVT, a modified Markov method, described for ZnSe:Ti by Klimakow *et al.* [10]), an additional TiS_2 source was arranged under the ZnS source, both were held at $T = 1417$ K. After four days growth, the massive crystals obtained were slowly cooled (at less than 30 K/h) to avoid cracking.

In the EPR work, a homodyne spectrometer was applied, here utilised in the X band. The samples were cooled by means of a flow cryostat, because the experiments required a temperature range from 3.4 to 80 K.

Optical measurements were performed in conventional spectroscopic setups, adapted to the necessities of low-temperature measurements in the near-infrared spectral region. Digital processing of the data included corrections for the spectral response of the apparatus.

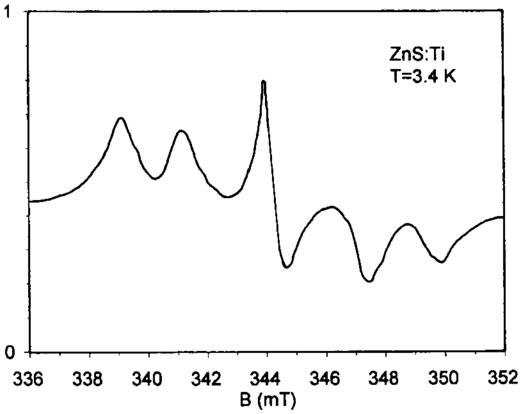

Fig. 2. EPR spectrum II of $Ti^{3+}(d^1)$ in ZnS, dynamic case ($T \cong 3.4$ K) at $\theta \sim 90°$, *i.e.* $B \parallel [110]$. The central line near 344 mT is the averaged signal. Because of their different saturation behaviour, spectra I and II are not observable under the same experimental conditions.

3 Results of the EPR experiments

In all three batches of crystals ("a, b, c"), Ti^{2+} was detected, in a and b Ti^{3+} in addition. While in b and c the Ti^{2+} resides exclusively in the tetrahedral environment of a substitutional cation lattice site, in charge "a" most of it is found in a hexagonal environment, oriented along the $[111]_W$ direction. The spectra chosen for presentation here have all been recorded with "a"-type samples for compatibility reasons. In addition to the various titanium spectra, the crystals employed show at $T = 3.4$ K traces of $Mn^{2+}(d^5)$, $Fe^{+}(d^7)$ and $Ni^{3+}(d^7)$. Furthermore, detectability of F^+ centres (anion vacancies) indicates a high position of the Fermi level.

The ^2D ground term of a free $Ti^{3+}(d^1)$ ion is split by the tetrahedral crystal field acting on a substitutional lattice site into a higher $^2T_2(D)$ level and a $^2E(D)$ ground state. Under coupling of e-type vibrations, this orbital doublet is further split into an upper Kramers doublet A_1, A_2 and a lower E-type state, separated by the tunneling splitting 3Γ. Owing to random internal strains, the ^2E vibronic state is finally broken up into two Kramers doublets in a mutual distance of approximately 1 cm^{-1} (Ham [13]), *cf.* Figure 12 in reference [12].

If the strain splitting $\delta \gg 3\Gamma$, the quasi-static limit is realised, like in the case of ZnSe:Ti^{3+}. The EPR spectrum (I) is between $T = 3.4$ and 30 K characterised by three structures of tetragonal (D_{2d}) symmetry, the principal axes oriented along the three $\langle 100 \rangle$ crystallographic axes of the ZnS crystal (Fig. 1a). Because of the presence of stacking faults (*cf.* Ref. [14]) and a small misalignment of the crystal, this spectrum is resolvable only along the [100] axis, yielding $g_{\parallel} = 1.827$ and $g_{\perp} = 1.962$. Small hyperfine-structure lines indicate interaction with ^{47}Ti and ^{49}Ti nuclei and entail a coupling constant $A_{\parallel} = 23 \times 10^{-4}$ cm^{-1}. In the $B \parallel \langle 111 \rangle_W$ direction, the lines coincide at $g_{\langle 111 \rangle} = 1.92$.

The second spectrum is also observable at $T = 3.4$ K, its two spin transitions show anisotropic g factors with a

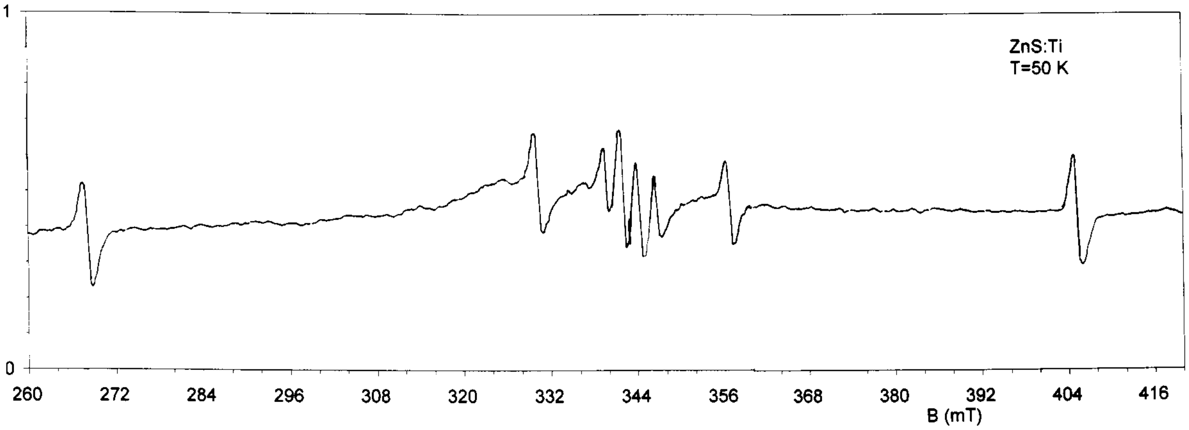

Fig. 3. EPR spectrum of Ti^{2+}, B at $\theta \cong 90°$ in $\{110\}$. $T \cong 50$ K. The signal at 344 mT marks Ti^{2+} on a cubic site, the corresponding Ti^{2+} spectrum of axial sites is the outermost doublet. The inner doublet and quartet represent the Ti^{2+}–Ti^{2+} pair spectra with $S = 1$ and $S = 2$, respectively.

$(1 - 3\cos^2\theta)$ variation (Fig. 1b) in the (110) plane. This finding is characteristic for dynamic Jahn-Teller transitions [13]:

$$h\nu_{\pm} = g_1\mu_B B \pm (1/2)qg_2\mu_B B(1 - 3\cos^2\theta)$$

where μ_B is the Bohr magneton and θ the direction cosine of B, relative to the $\langle 100\rangle$ axes. For the spectrum of Figure 2 this relationship yields $g_1 = 1.9297$, $-qg_2 = 0.0342$, with the reduction factor $q = 0.47$, pointing towards a strong linear Jahn-Teller coupling with only slight warping, while for ZnSe:Ti $q = 0.38$ resulted, *cf.* reference [12]. With increasing temperature, this anisotropic spectrum (II) changes into an isotropic spectrum with an average $g = 1.9297$, indicating rapid vibronic relaxation between the strain-split ground-state components [15]. This typical dynamic spectrum is observed up to 15 K while the quasi-static spectrum (I) is still visible at $T = 30$ K. The fact that both the static and the dynamic spectra occur at temperatures as low as 3.5 K points towards a very small strain splitting of the ^2E doublet, in other words, like with Ti^{3+} in ZnSe, the first excited vibronic state is very close to the ground level.

In addition to the spectra I and II of Ti^{3+} just described, there exists still a third one, featuring an isotropic $g = 1.928$ (Fig. 3). It is strongly saturated at $T = 3.5$ K but observable up to $T = 80$ K. At higher microwave power the main structure is a sharp $\Delta M_S = 2$ double-quantum transition, superimposed on a broader $\Delta M_S = 1$ resonance. This behaviour is characteristic for a spin triplet ($S = 1$), *cf.* reference [1]. Ti^{2+} is known to undergo a threefold splitting of its ^3F free-ion ground term if exposed to a tetrahedral (T_d) crystal field, with $^3T_1(F)$, $^3T_2(F)$ and $^3A_2(F)$ levels emerging. The latter manifold forms the ground state and has the properties required when the ion occupies a cubic AN site (nomenclature of Ref. [14]). In the same temperature range, additional strong Ti^{2+} signals are found, this time corresponding to ions in a stacking-faulted environment with lower local symmetry (C_{3v}), *i.e.* on axial sites (PN and AS). The number of lines and their angular dependence can be described by an axial spin-Hamiltonian with $S = 1$. Two lines with a $(1 - 3\cos^2\theta)$ angular dependence are assigned to $\Delta M = \pm 1$ transitions. The third one is caused by the "forbidden" transition with $\Delta M = \pm 2$. At $B \parallel \langle 111\rangle_W$ and $B \perp \langle 111\rangle_W$, the g factor was determined as $g_{\parallel} = 1.976$, $g_{\perp} = 1.969$ and the zero-field splitting as $D = 0.127\ \mathrm{cm}^{-1}$.

Two additional signals with the same angular variation are recorded (Fig. 4), a doublet with a 1:1 peak ratio and a quartet with the ratios 2:3:3:2. They are assigned to Ti^{2+}–Ti^{2+} pair spectra on axial sites, aligned along the $[111]_W$ direction, and characterised by $g = 1.926$, zero-field splitting $D_1 = 268$ mT and $D_2 = 2.4$ mT. On pairing, the $S = 1$ ground state of a single Ti^{2+} ion entails formation of pairs with $S = 0, 1, 2$. Consequently, the detected doublet represents $S = 1$ and the quartet likewise $S = 2$.

Charge conversion from Ti^{2+} to Ti^{3+} requires a minimum energy of $15\,000\ \mathrm{cm}^{-1}$ approximately. Thus it can efficiently be accomplished by orange or even red irradiation of the crystal (using Schott filters OG 3 or RG 3, respectively) while the $27\,400\ \mathrm{cm}^{-1}$ radiation of a high-pressure Hg lamp would favour Ti^{2+} (Fig. 5). This transformation is also effected by above-band-gap irradiation. The Ti^{2+} signals thus produced are stable after the light is switched off. A previous red-light-induced shift of the balance towards Ti^{3+} is reversed under these conditions, and the $[\mathrm{Ti}^{2+}]/[\mathrm{Ti}^{3+}]$ concentration ratio restored to its earlier value. A more detailed insight into these processes will be gained from the optical studies to be described in Section 5.

4 "Internal" optical transitions within Ti^{2+} and Ti^{3+} centres

While some examples of previous EPR and optical absorption studies on Ti^{2+} are quoted in the Introduction, neither the existence of Ti^{3+} centres nor any "internal" luminescence processes of titanium ions had been detected

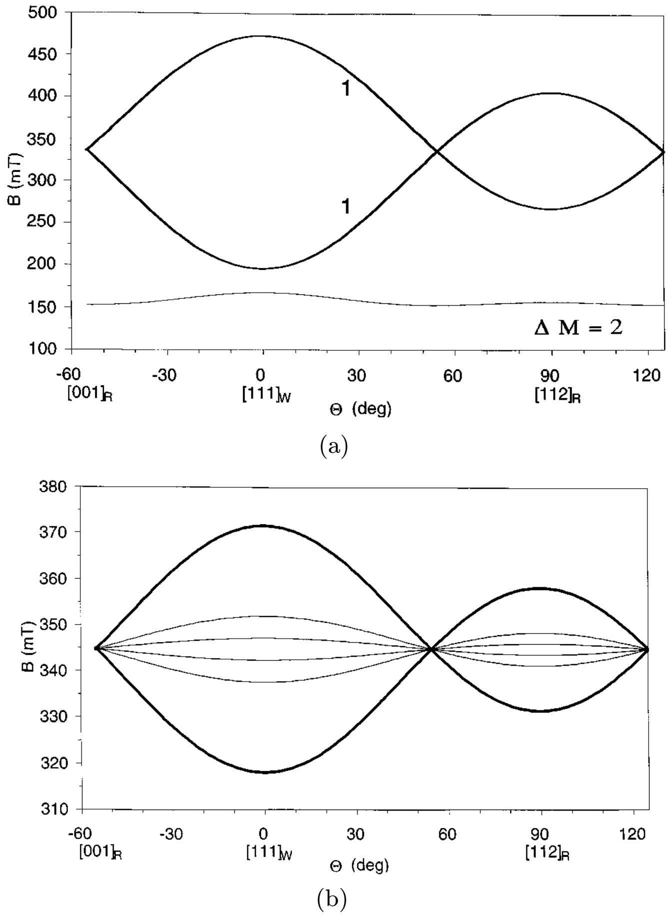

(a)

(b)

Fig. 4. Angular dependence of (a) the axial Ti^{2+} EPR signal and (b) the EPR spectrum of the Ti^{2+}–Ti^{2+} pairs (outer doublet: $S = 1$, inner quartet: $S = 2$).

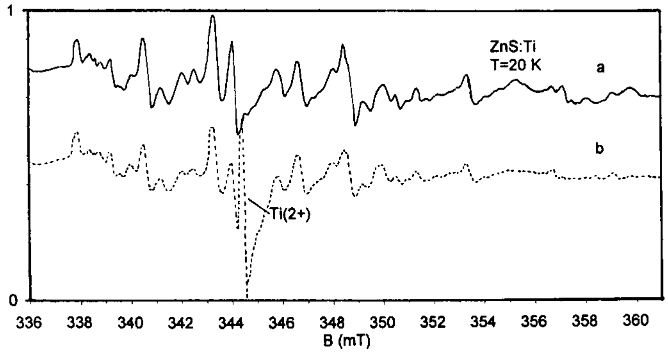

Fig. 5. $Ti^{2+} \Leftrightarrow Ti^{3+}$(spectrum I, *i.e.* static signal) charge conversion as detected by EPR. Trace a: "red" irradiation, trace b: near-edge irradiation.

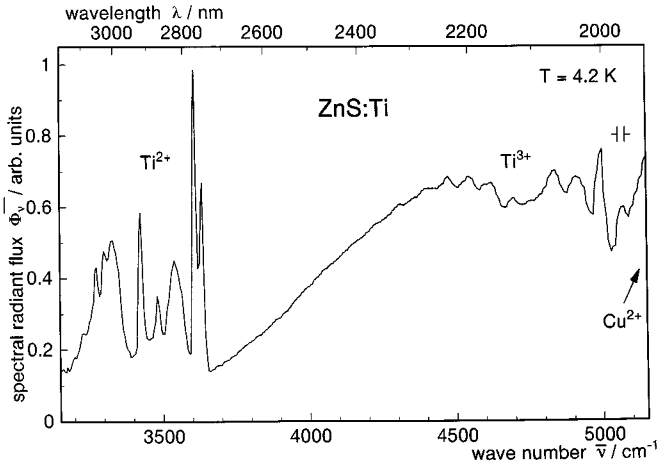

Fig. 6. Emission survey of ZnS:Ti at $T \cong 4.2$ K (charge a, estimated Ti concentration in the crystal: 1500 ppm) under excitation in the interval 13 300 cm^{-1} to 33 000 cm^{-1}. Above 5000 cm^{-1}, the low-energy tail of the Cu^{2+} emission (*cf.* Ref. [23]) is visible.

until 1994. Up to that time, emission was investigated only in the near-edge region where excitonic transitions and donor-acceptor recombination prevail [16,17].

By absorption spectroscopy with II-VI semiconductors, up to three bands of Ti^{2+} could be elicited, depending on the material, but irrespective of the degeneracy with the conduction bands in some of them. These observed transitions lead from the $^3A_2(F)$ ground state to the $^3T_1(P)$, $^3T_1(F)$, and $^3T_2(F)$ levels (order of decreasing energy). In the present study, the individual emission spectra of titanium ions in their different oxidation states in ZnS will be identified for the first time and will then serve as probes of the presence or absence of the respective centres. The transitions involved are $^3T_2(F) \rightarrow {}^3A_2(F)$ of $Ti^{2+}(d^2)$ and $^2T_2(D) \rightarrow {}^2E(D)$ of $Ti^{3+}(d^1)$.

All crystals produced in this study exhibit a brown colour, those of batch a are tinted most intensely. Like the EPR data, the presented optical spectra were recorded with "a"-type samples since these display the strongest luminescence. The arising complications in the structure of the spectra are compensated by the ensuing consistency of optical and EPR results.

Under broad-band excitation at low temperature, charge "a" crystals exhibit two emission bands (Fig. 6). The strongly-structured photoluminescence of Ti^{2+} is similar to that of ZnSe:Ti [10]. The broad Ti^{3+} emission also resembles those in ZnSe [10], CdS and CdSe [18] and (Cd,Zn)Te [11]. The assignment of these bands to the given oxidation states rests on the mentioned analogy with EPR in their appearing in different specimens, the details of the excitation spectra (see below) and the common reasoning which predicts a larger crystal-field splitting for d^1 than d^2, based on smaller screening of the ligand field.

A shape analysis of the overall emission appearance (Fig. 7) reveals a striking similarity with the one-phonon density-of-states for cubic ZnS [19]. Simple phonon-assisted transitions are thus proved to prevail in the side bands. The situation is similar to the case of the $Co^{2+}(d^7)$ ion (*cf.* Ref. [20]) which has a one-dimensional A_2 ground state in T_d as well. The sole exception seems to be the 3484 cm^{-1} peak which is thus shown to be either a local impurity mode or a two-phonon TA(L) satellite of a hexagonal environment. Other prominent spectral features include: the cubic TA(L) at 3540, LA(L) at 3425,

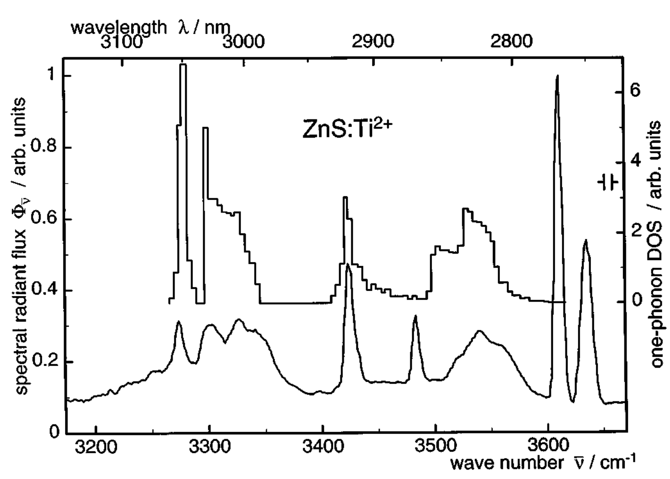

Fig. 7. Comparison of Ti^{2+} emission (lower trace, *cf.* Fig. 6) with one-phonon density-of-states (upper trace, after Kunc [19]).

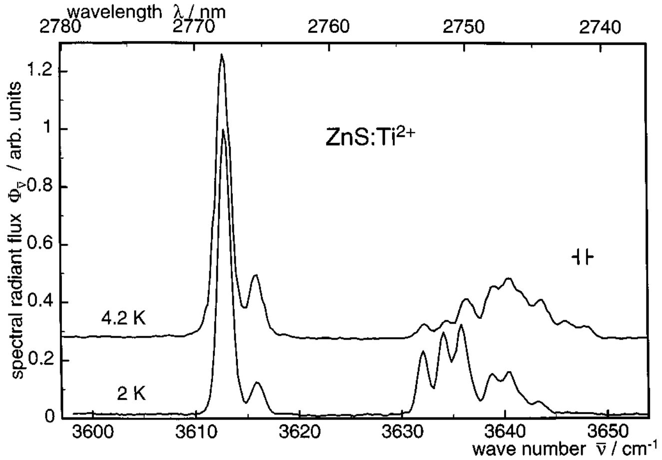

Fig. 8. Spectrum of the $^3T_2(F) \rightarrow {}^3A_2(F)$ emission of Ti^{2+} in ZnS at two different temperatures (charge "a" crystal); excitation at 21 837 cm^{-1}.

TO(X) at 3302 and LO(L) at 3274 cm^{-1}, moreover the hexagonal TA(L) at 3560 and TO at 3344 cm^{-1}.

For an interpretation of the fairly complicated no-phonon region, a study of the spectral evolution with a temperature rise is helpful (Fig. 8). Evidently thermalisation, *i.e.* occupation of higher sublevels on increasing temperatures, arises for both the ground and excited states involved. The components of d^2 crystal-field levels are subject to spin-orbit coupling but to Jahn-Teller effect as well, details have been studied, *e.g.*, with the isoelectronic V^{3+} ion (*cf.* Ref. [21]). According to these deliberations, from the spin-orbital components of the initial $^3T_2(F)$ state, a higher sextet $\Gamma_4 + \Gamma_5$ and a lower quartet $\Gamma_2 + \Gamma_3$ would emerge under JT interaction with e modes while the $^3A_2(F)$ ground level yields a Γ_5 in T_d symmetry. From this ground level, three components are derived in trigonal symmetry, from the higher levels a manifold of descendents would arise. The prominent line at 3613 cm^{-1} is now assigned to the cubic main transition, the 3616 cm^{-1} satellite to its thermalised companion (initial-state splitting), and the transitions at 3636, 3634, and 3632 cm^{-1} to centres in various trigonally distorted environments, as corroborated by the EPR data. The structures at and beyond 3639 cm^{-1} are thermalised satellites of the trigonal transitions.

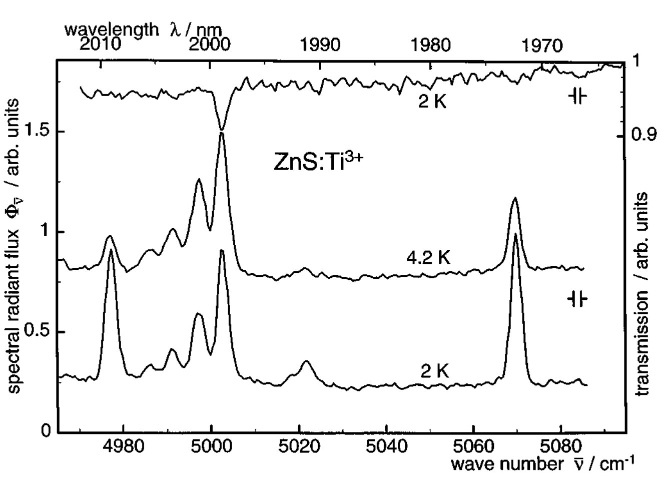

Fig. 9. Spectrum of the $^2T_2(D) \rightarrow {}^2E(D)$ emission of Ti^{3+} in ZnS at two different temperatures (charge "a" crystal); excitation at 21 837 cm^{-1}. Uppermost trace: transmission at 2 K for comparison.

The weak Ti^{3+} emission is superimposed onto the tail of the high-energy Cu^{2+} emission (*cf. e.g.* Refs. [22, 23]). Like Ti^{2+}, Ti^{3+} occurs in two different environments in ZnS (Fig. 9). The cubic main line is situated at 5070 cm^{-1}. Further cubic lines are found at 5022, 5018, and 4977 cm^{-1}. The structures at 5003, 4997, 4991, and 4986 cm^{-1} are assigned to trigonal centres, since the $\Gamma_8 -{}^2E(D)$ ground level is split into four components under a trigonal distortion. Their relative strength increases with the temperature, possibly involving cross-relaxation from the higher-lying cubic initial levels (*cf.* Ref. [24]). An emission doublet at 4787 and 4771 cm^{-1} points to an interpretation as TO satellites of the 5070 cm^{-1} principal line and a barely visible absorption transition at 5085 cm^{-1} which is thus also attributed to a cubic centre. A detailed analysis of the level structure must go beyond simple crystal-field reasoning including spin-orbit splittings, it can only be expected on the basis of the Jahn-Teller interactions indicated by the EPR findings.

The excitation spectrum (Fig. 10) of the $Ti^{2+}(d^2)$ emission (*cf.* Figs. 6–8) allows a clear distinction between the two narrow internal bands at the lower-energy end and the broader charge-transfer region towards higher energies. The 10 400 cm^{-1} band was earlier detected in absorption [9] and plausibly assigned to the transition terminating in $^3T_1(P)$. Its full-width at half-maximum (FWHM: 900 cm^{-1}) is determined by spin-orbit and Jahn-Teller effects like that of the even wider band (1400 cm^{-1}) of the transition to $^3T_1(F)$ near 6200 cm^{-1}. While the region closely above 11 500 cm^{-1} seems to be influenced by Cu-related transitions (*cf.* Ref. [23]), a strong charge-transfer band starts near 22 000 cm^{-1} which is related to reaction

Table 1. Magnetic properties of ZnS:Ti as determined from EPR.

spectrum	g value	zero-field splitting (10^{-4} cm^{-1})	hyperfine splitting: ^{47}Ti, ^{49}Ti (10^{-4} cm^{-1})
Ti^{3+} (spectrum I) $T = 3.4$ K	$g_{\parallel} = 1.827 \pm 0.001$ $g_{\perp} = 1.962 \pm 0.001$		$A_{\parallel} = 23$
Ti^{3+}(spectrum II) $T = 3.4$ K	$g_1 = 1.9297 \pm 0.0006$ $-qg_2 = 0.0171$ $q = 0.47$		
Ti^{2+} (T_d) $T = 50$ K	$g = 1.9280 \pm 0.0006$		
Ti^{2+} (axial: C_{3v}) $T = 50$ K	$g_{\parallel} = 1.976 \pm 0.001$ $g_{\perp} = 1.969 \pm 0.001$	$D = 1270 \pm 10$	
Ti^{2+} (pair sp.) axial $\langle 111 \rangle_W$ $T = 50$ K	$g_0 = 1.926 \pm 0.001$	$D_1 = 241$ $D_2 = 21.6$	

Table 2. Charge-transfer processes and internal transitions (2 and 4) included into the one-particle model of Figure 14. In the reaction schemes, an asterisk (*) marks an excited state of the respective ion, *cb* and *vb* indicate the conduction and valence bands, respectively. t_2 and e represent the corresponding orbitals, with the usual notation of exponents representing the occupation numbers. For summation (reaction 5, resulting from addition of reactions 3 and 4) and difference processes (reaction 10, obtained by subtraction of 4 from 8), see text.

process	reaction		
1	$\text{Ti}^{3+}(e) + h\nu$ (22 000 cm^{-1})	$\Leftrightarrow$	$[\text{Ti}^{2+}]^*(t_2e) + e^+_{vb}$
2	$[\text{Ti}^{2+}]^*(t_2e)$	$\Leftrightarrow$	$\text{Ti}^{2+}(e^2) + h\nu$ (3600 cm^{-1})
3	$\text{Ti}^{2+}(e^2) + h\nu$ (12 900 cm^{-1})	$\Leftrightarrow$	$\text{Ti}^{3+}(e) + e^-_{cb}$
4	$\text{Ti}^{3+}(e) + h\nu$ (5100 cm^{-1})	$\Leftrightarrow$	$[\text{Ti}^{3+}]^*(t_2)$
5	$\text{Ti}^{2+}(e^2) + h\nu$ (18 000 cm^{-1})	$\Rightarrow$	$[\text{Ti}^{3+}]^*(t_2) + e^-_{cb}$
6	$[\text{Ti}^{2+}]^*(t_2e) + e^+_{vb}$	$\Rightarrow$	$[\text{Ti}^{3+}]^*(t_2) + h\nu$ (16 900 cm^{-1})
7	$[\text{Ti}^{2+}]^*(t_2e) + h\nu$ (14 400 cm^{-1})	$\Rightarrow$	$[\text{Ti}^{3+}]^*(t_2) + e^-_{cb}$
8	$\text{Ti}^{3+}(e) + h\nu$ (18 400 cm^{-1})	$\Leftrightarrow$	$\text{Ti}^{2+}(e^2) + e^+_{vb}$
9	$[\text{Ti}^{2+}]^*(t_2e) + h\nu$ (9300 cm^{-1})	$\Leftrightarrow$	$\text{Ti}^{3+}(e) + e^-_{cb}$
10	$\text{Ti}^{2+}(e^2) + e^+_{vb}$	$\Rightarrow$	$[\text{Ti}^{3+}]^*(t_2) + h\nu$ (13 300 cm^{-1})

1 in Table 2. The first excited state of Ti^{2+} is directly created from the Ti^{3+} ground state, followed by the radiative relaxation according to reaction 2 (Tab. 2).

The excitation of the Ti^{3+}(d^1) internal luminescence (Fig. 11) is again dominated by a strong crystal-field band near 5700 cm^{-1}. Since the overlap of the Ti^{3+} emission with the Cu^{2+} emission impedes a separate measurement of both these excitation spectra, the Cu acceptor transition commencing at 10 500 cm^{-1} and a shoulder near 7000 cm^{-1} caused by the Cu^{2+} internal absorption are residual artefacts in the spectrum of Figure 11. On the other hand, the Cu^{2+} excitation spectrum taken with the same crystal does not show any of the Ti characteristics, thus excluding an appreciable energy transfer from titanium to copper. The broad band with onset at 22 000 cm^{-1} familiar from the Ti^{2+} excitation spectrum (*cf.* Fig. 10) is likewise seen in the Ti^{3+} spectrum of Figure 10. Evidently, de-excitation of the [Ti^{2+}]* excited state is not only feasible by reaction 2 of Table 2 but also *via* recapture of the hole generated in process 1, followed by Ti^{3+} luminescence (reactions 6, 4).

5 Charge-transfer transitions connecting Ti^{2+} and Ti^{3+} states and their visualisation in a one-particle model

In discussing the excitation processes in Section 4, it became clear that some of the occurring sequences (*e.g.* reactions 1 - 6 - 4 of Tab. 2) involved conversions of the oxidation states of the Ti centres. An additional means of disentangling the sometimes complicated interplay between various charge states is the recording of sensitisation

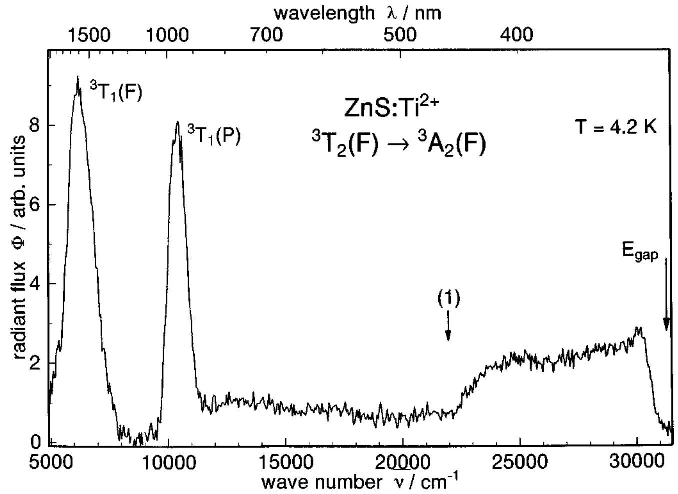

Fig. 10. Excitation spectrum of the $^3T_2(F) \rightarrow {}^3A_2(F)$ luminescence of $Ti^{2+}(d^2)$ at $T = 4.2$ K. Emission detected in the range 3100–3900 cm^{-1}. The pointer (1) refers to the onset of reaction 1 in Table 2.

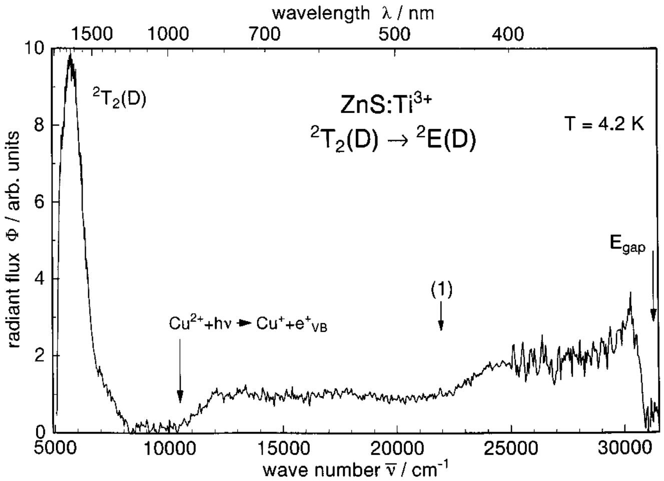

Fig. 11. Excitation spectrum of the $^2T_2(D) \rightarrow {}^2E(D)$ luminescence of $Ti^{3+}(d^1)$ at $T = 4.2$ K. Emission detected in the range 3850–4760 cm^{-1}. The pointer (1) marks the onset of reaction 1 (*cf.* Tab. 2).

and/or quenching spectra. Here, the influence of an auxiliary irradiation onto the sample by an extra light source is plotted *versus* its spectral position. The specific influence of this "pumping" light beam is separated from the modulated primary excitation by utilising unmodulated light which is not detected directly by the employed a.c. lock-in amplifiers. Detected is, however, the change in the state of the specimen brought about by the secondary beam. This state is, in our case, given by the relative concentrations of impurities in the charge states involved. Their presence is probed by the luminescence excited by the primary beam.

At a relatively low primary excitation energy, the influence of additional light is expected to be in general most clearly detectable. The energy of 6000 cm^{-1} was chosen since it would excite both Ti^{2+} and Ti^{3+} by internal transitions, *cf.* excitation spectra (Figs. 10 and 11).

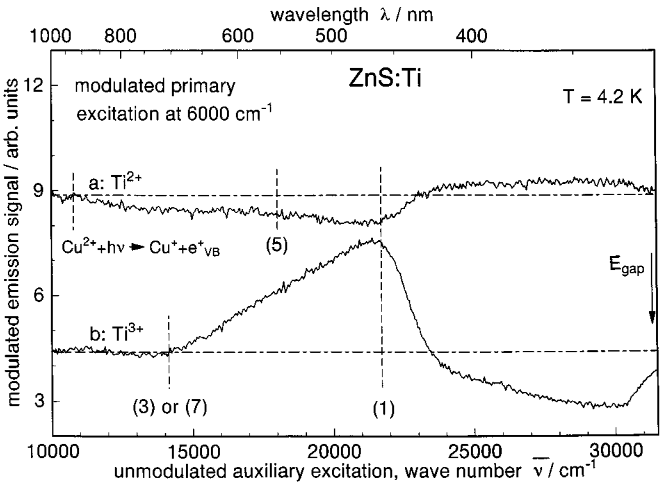

Fig. 12. Sensitisation and quenching of the Ti^{2+} emission (trace "a", detected in the 3100–3900 cm^{-1} range) and the Ti^{3+} emission (trace "b", detected in the interval 3850–4760 cm^{-1}), both under modulated 6000 cm^{-1} primary excitation at $T = 4.2$ K.

The respective sensitisation spectra (Fig. 12) have pronounced countercurrent tendencies although the Ti^{2+} luminescence is influenced to a smaller extent than the Ti^{3+} emission, probably because of a smaller number of available Ti^{3+} centres. At 10 500 cm^{-1}, hole generation at Cu centres is manifested in the Ti^{2+} spectrum (upper trace) as a quenching of the emission process 2 by reactions 6 and 8 of Table 2, both creating Ti^{3+} at the expense of Ti^{2+} luminescence. Above 14 000 cm^{-1} the Ti^{3+} signal is strongly stimulated, this time by generation of conduction electrons from Ti^{2+} by processes 3 or 7. Although 7 is an excited-state absorption, it cannot be excluded from the outset because of the expected long lifetime of the Ti^{2+} $^3T_2(F)$ state whose radiative relaxation is electric-dipole-forbidden. Analogy with ZnSe:Ti [12] and the numerical estimates support interpretation of this threshold by reaction 7 indeed. Finally, an onset of process 1 near 22 000 cm^{-1} favours Ti^{2+} so that the Ti^{3+} sensitisation is impaired accordingly.

A different situation (Fig. 13) arises if the primary radiation is fixed in a spectral region where a constant hole generation is achieved by the Cu acceptor absorption marked in Figure 11. Recapture of a hole entails consecutive infrared Cu^{2+} emission. An increase of the photon energy beyond 14 500 cm^{-1} will produce electrons in the CB, and all three emission bands monitored in the spectra of Figure 13 are sensitised. Only above 22 000 cm^{-1}, the Ti^{2+} and Ti^{3+} behaviours are differentiated, as known already from the findings in Figure 12. Under these conditions, again holes are created in the VB by reaction 1, Table 2, titanium ions are neutralised and the copper balance is pushed towards the lattice-neutral charge state as well. The opposite tendencies in the Ti^{3+} and Cu^{2+} curves proof that the Cu^{2+} tail has been well suppressed while recording the Ti^{3+} emission.

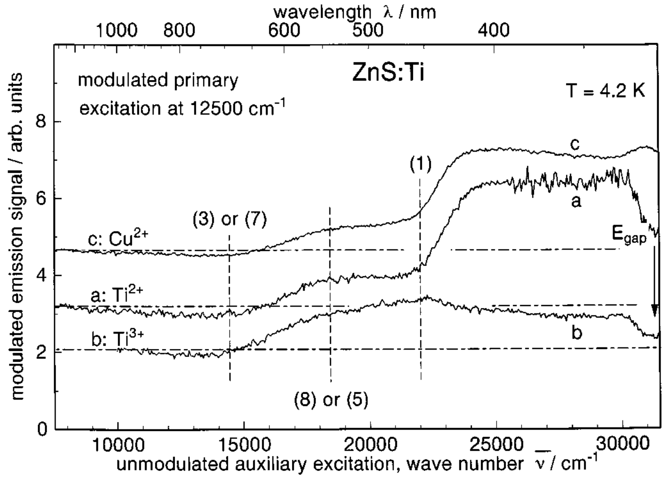

Fig. 13. Sensitisation (and some quenching) at $T = 4.2$ K of (a) the Ti^{2+} emission (detected between 3100 and 3900 cm^{-1}), assembled from two parts, matched at 26 000 cm^{-1}. (b) The Ti^{3+} emission (detected between 3850 and 4760 cm^{-1}), (c) the Cu^{2+} emission (detected between 5000 and 7200 cm^{-1}). 1, 3, 5, 7 and 8 label the corresponding reactions in Table 2.

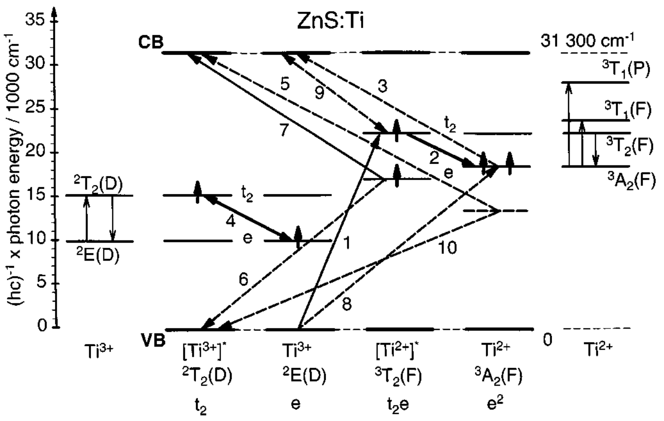

Fig. 14. One-particle model of $\mathrm{Ti}^{2+}(d^2)$ and $\mathrm{Ti}^{3+}(d^1)$ ions in ZnS, in their ground and first excited states. Full lines mark observed electron transitions, broken lines some further predicted transitions as derived from the processes discussed. The arrows are designated according to the numbers of the reactions included in Table 2. Corresponding many-electron states are indicated near the left and right margins for comparison.

The temporal evolution of charge conversions could be followed during the described processes since changes occur with time constants of some seconds. Under 10 450 cm^{-1} excitation, a crystal cooled in the dark exhibits a Ti^{2+} signal of 60 μV which would decrease to 8 μV under "red" irradiation ($\bar{\nu} \leq 16\,400\ \mathrm{cm}^{-1}$) and increase to 190 μV on subsequent UV irradiation ($\bar{\nu} \approx 27\,000\ \mathrm{cm}^{-1}$). The concentration of Ti^{2+} remains frozen under steady primary excitation after the auxiliary red or UV light has been switched off. These findings correspond to those reported in Section 3 for the EPR signals.

The processes discussed here and in the previous sections have been compiled in Table 2 and are also depicted in a one-particle model for the titanium ground and (lowest) excited states (Fig. 14), as earlier proposed and applied to the case of Ti in ZnSe [12]. The model comprises the t_2 and e states of impurity electrons in a tetrahedral crystal field, each of the four states Ti^{2+}, $[\mathrm{Ti}^{2+}]^*$, Ti^{3+}, $[\mathrm{Ti}^{3+}]^*$ represented by a column, ordered by increasing number of electrons. While full arrows indicate observed processes, broken arrows represent such transitions which are indirectly inferred from the reactions described in Table 2. In this sense, they are no less real than those of the full arrows. The graph symbolises a considerable body of empirical material contained in the above-given data and discussed in their appropriate context. Nevertheless the model, as any image of nature, still contains some ambiguity in details of the interpretations.

A material implication of the findings is the necessity to attach more than one energy level to each state of the impurity ion. This is an almost trivial consequence of the crystal-field splitting of d electron states into the threefold degenerate t_2 and the twofold e levels. But it is also empirically demonstrated here by reactions 1 and 7 which imply these different levels ascribed to the $[\mathrm{Ti}^{2+}]^*$ centre. Less straightforward is the assumption of the so-called sum process 5, as obtained by addition of reactions 3 and 4. Its appearance is disclosed in Figures 12 and 13 by the spectral features marked with 5. The corresponding situation holds for the difference process 10 of Table 2 which is obtained by subtracting reaction 4 from reaction 8. The model of Figure 14 can be adapted to this concept by adding a "virtual" level to the ladder of Ti^{2+} energy states. While an incorporation of summation and difference reactions does not seem to be indispensible here, they were included for comparison.

6 Discussion

The overall picture of the experimental data comprises information on (i) the individual ions $\mathrm{Ti}^{2+}(d^2)$ and $\mathrm{Ti}^{3+}(d^1)$ whose presence has been proved independently and consistently by EPR and optical methods, preferentially based on luminescence, (ii) a variety of processes which relate these oxidation states and demonstrate their mutual convertibility, mainly induced by optical irradiation of the samples. It should be stressed that the conceptually simpler ion Ti^{3+} with its d^1 configuration is governed by quite sophisticated Jahn-Teller interaction.

The observed NPL positions of the cubic Ti^{2+} and Ti^{3+} centres in ZnS fit convincingly into the pattern derived from the findings with other II-VI compounds [25]. In these considerations, the simplifying assumption is made implicitly that the experimental level distances represent the crystal-field splitting of 10 Dq between the lowest energy levels participating in optical transitions. The resulting trends are similar to those earlier obtained for vanadium [26] and nickel ions [25].

In an early example of a refined interpretation of d^2 crystal field splitting in CdTe:Ti, Biernacki and Schulz [27] considered the stronger repulsive influence of ligand electrons on the radial extension of t_2 type orbitals compared with e orbitals. The derived values for the crystal field parameter Dq emerged smaller if the repulsion energy was taken into account in treating previous experimental data [3,28].

While the fine-structure details of EPR data require a more elaborate model (*cf.* Fig. 12 of Ref. [12]) including spin-orbit and Jahn-Teller effects, the bulk of the optical findings becomes comprehensible in a comparatively simple one-particle model (*cf.* Fig. 14 of the present paper) where the various oxidation or excitation states of Ti are represented by the appropriate groups of t_2- and e-type crystal-field levels. In particular, the donor energy is read from reaction 3 (Tab. 2) as 12 900 cm^{-1}, *cf.* Figure 14. The corresponding values are 8500 cm^{-1} for ZnSe [12] and 12 300 cm^{-1} for ZnTe [25]. These ionisation energies harmonise well with the idea [29] that the different photoionisation energies of a 3d impurity in the same class of semiconducting materials can be applied to arrange the host lattice bands so as to obtain a common reference level. Based on a collection of empirical data, Langer *et al.* [30] elaborated this scheme for the III-V and II-VI compounds. The above given numbers derived in the present study imply downward shifts of 600 and 4400 cm^{-1} for the CB minima of ZnTe and ZnSe, respectively, while the predicted shifts are 200 and 4100 cm^{-1}, referred to the ZnS VB maximum as a lower normalisation energy. In regard of the experimental error of approximately 800 cm^{-1} in the determination of charge-transfer energies, this agreement is striking.

Some preliminary results of the present work were reported recently at a meeting [31]; the salient features of the work formed the base of a poster at the 16th General Conference of the Condensed Matter Division of the EPS in Leuven, Belgium, August 1997 (unpublished). Fruitful discussions with S.W. Biernacki, Warszawa, J. Kreissl and H.R. Selber, both Berlin, contributed to the interpretation of the results.

References

1. J. Schneider, A. Räuber, Phys. Lett. **21**, 380 (1966).
2. J. Dziesiaty, R. Böttcher, Phys. Stat. Sol. **26**, K21 (1968).
3. R.K. Watts, Phys. Lett. A **27**, 469 (1968).
4. R. Boyn, J. Dziesiaty, D. Wruck, Phys. Stat. Sol. **42**, K197 (1970).
5. E.M. Wray, J.W. Allen, J. Phys. C: Solid State Phys. **4**, 512 (1971).
6. K. Kocot, J.M. Baranowski, Phys. Stat. Sol. (b) **59**, K11 (1973).
7. K. Kocot, J.M. Baranowski, Phys. Stat. Sol. (b) **81**, 629 (1977).
8. J. Gardavsky, I. Barvik, M. Zvara, Phys. Stat. Sol. (b) **84**, 691 (1977).
9. J.M. Baranowski, J.M. Noras, J.W. Allen, Proc. 12th Int. Conf. Physics of Semiconductors, Stuttgart 1974, p. 416.
10. A. Klimakow, J. Dziesiaty, J. Korostelin, M.U. Lehr, P. Peka, H.-J. Schulz, Advd. Mater. Opt. Electron. **3**, 253 (1994).
11. P. Peka, M.U. Lehr, J. Dziesiaty, S. Müller, J. Kreissl, P. Rudolph, H.-J. Schulz, Mater. Sci. Forum **143-147**, 435 (1994).
12. J. Dziesiaty, P. Peka, M.U. Lehr, H.-J. Schulz, A. Klimakow, Phys. Rev. B **49**, 17 011 (1994).
13. F.S. Ham, in *Electron Paramagnetic Resonance*, edited by S. Geschwind (New York: Plenum, 1972), p. 1.
14. T. Buch, B. Clerjaud, B. Lambert, P. Kovacs, Phys. Rev. B **7**, 184 (1973).
15. J.R. Herrington, L.A. Boatner, T.J. Aton, T.L. Estle, Phys. Rev. B **10**, 833 (1974).
16. R.V. Gamernik, Yu.P. Gnatenko, A.S. Krochuk, Z.S. Poslavskij, Ukr. Fiz. Zh. **33**, 1167 (1988).
17. P.I. Babii, V.V. Slynko, Yu.P. Gnatenko, P.N. Bukivskii, M.I. Ilashchuk, O.A. Parfenyuk, Fiz. Tekh. Poluprovodn. **24**, 1444 (1990); Sov. Phys. Semicond. **24**, 904 (1990).
18. P. Peka, M.U. Lehr, H.-J. Schulz, J. Dziesiaty, S. Müller, J. Crystal Growth **161**, 277 (1996).
19. K. Kunc, Ann. Phys. Fr. **8**, 319 (1973/74).
20. H.-J. Schulz, Mater. Chem. Phys. **16**, 373 (1987).
21. G. Aszódi, U. Kaufmann, Phys. Rev. B **32**, 7108 (1985).
22. H.-J. Schulz, Phys. Stat. Sol. **3**, 485 (1963).
23. P. Peka, H.-J. Schulz, Physica B **193**, 57 (1994).
24. F. Fuchs, P. Koidl, Solid State Commun. **87**, 791 (1993).
25. H.R. Selber, P. Peka, H.-J. Schulz, U.W. Pohl, J. Kreissl, B. Kaufmann, A. Dörnen, ICDS 19, Aveiro, Portugal; Mater. Sci. Forum **258-263**, 1401 (1997).
26. P. Peka, H.R. Selber, H.-J. Schulz, R. Schwarz, K.W. Benz, Solid State Commun. **98**, 677 (1996).
27. S.W. Biernacki, H.-J. Schulz, Phys. Stat. Sol. (b) **103**, K163 (1981).
28. P.A. Slodowy, J.M. Baranowski, Phys. Stat. Sol. (b) **49**, 499 (1972).
29. L.A. Ledebo, B.K. Ridley, J. Phys. C **15**, L961 (1982).
30. J.M. Langer, C. Delerue, M. Lannoo, H. Heinrich, Phys. Rev. B **38**, 7723 (1988).
31. P. Peka, M.U. Lehr, A. Klimakow, H.-J. Schulz, Verhandl. DPG **31**, 1438 (1996).